X-ray micro-computed tomography-based approach to estimate the upper limit of natural H2 generation by Fe2+ oxidation in the intracratonic lithologies

Kanchana Kularatne, Pascale Sénéchal, Valentine Combaudon, Othmane Darouich, Maria Angels Subirana, Arnaud Proietti, Caroline Delhaye, Dirk Schaumlöffel, Olivier Sissmann, Eric Deville, et al.

International Journal of Hydrogen Energy 78 (2024) 861–870

Contents lists available at ScienceDirect

International Journal of Hydrogen Energy

journal homepage: www.elsevier.com/locate/he

X-ray micro-computed tomography-based approach to estimate the upper limit of natural H_2 generation by Fe^{2+} oxidation in the intracratonic lithologies

Kanchana Kularatne [a,b,*], Pascale Sénéchal [b], Valentine Combaudon [a,c,d], Othmane Darouich [b], Maria Angels Subirana [e], Arnaud Proietti [f], Caroline Delhaye [g], Dirk Schaumlöffel [e], Olivier Sissmann [c], Eric Deville [c], Hannelore Derluyn [a,b]

[a] Universite de Pau et des Pays de l'Adour, E2S UPPA, CNRS, LFCR, Pau, France
[b] Universite de Pau et des Pays de l'Adour, E2S UPPA, CNRS, DMEX, Pau, France
[c] IFP Energies Nouvelles, 1- 4 Avenue du Bois Préau, 92852, Rueil-Malmaison, France
[d] Department of Geological Sciences, University of Colorado, Boulder, CO, 80309, USA
[e] Universite de Pau et des Pays de l'Adour, CNRS, Institut des Sciences Analytiques et de Physico-Chimie pour l'Environnement et les Matériaux (IPREM), UMR 5254, Helixoparc, 2 Avenue Pierre Angot, Pau, France
[f] Centre de Microcaractérisation Raimond Castaing, 3 Rue Caroline Aigle, 31400, Toulouse, France
[g] Universite Bordeaux 1, Institut des Sciences Moléculaires (ISM) UMR 5255, 351 Cours de la libération, 33405, Talence, Cedex, France

ARTICLE INFO

Handling Editor: Dr A Iranzo

Keywords:
Correlative imaging
Fluid-rock interactions
Igneous rock monzo-diorite
Kansas

ABSTRACT

Natural hydrogen (H_2) emanations in intracratonic areas offer potentially exploitable carbon-free energy. To date, H_2 seepages have been detected in more than sixty sites with exploration ongoing in many locations. One mechanism of natural hydrogen generation is the oxidation of Fe^{2+} in Fe-rich lithologies, and estimating the potential for hydrogen generation by this pathway is an important aspect of characterizing H_2-generating rocks. However, accurate estimation of Fe^{2+} can be challenging due to large-scale heterogeneities and small sample sizes used in conventional analysis. Here, we propose a correlative imaging technique to assess H_2 generation potential in Fe^{2+}-rich source rocks by integrating 2D chemical information with 3D volumes of the rock imaged using X-ray computed tomography (micro-CT). The advantage of this method lies in its ability to analyze a whole drill core of the source rock to obtain the most representative values while preserving sample integrity. Our method, validated on fractured monzo-diorite from a natural H_2-emitting well in Kansas, USA, yields an estimate of 707.93 ± 49.18 mol (H_2)/ton (source rock), as the upper limit. The proposed method could be useful in characterizing source rocks and estimating their natural H_2 generation potential in the early stages of natural H_2 exploration.

1. Introduction

Natural hydrogen is getting important as it could potentially offer carbon-free energy [1–5]. The largest quantity of natural H_2 on the Earth is generated in the ocean floor, along the tectonically active mid-oceanic ridges due to the hydrothermal alteration of ultramafic oceanic crust, that serves as the major energy source for deep life to thrive [6–10] while providing reducing conditions necessary for abiotic synthesis of organic molecules [10–15]. However, natural H_2 emanations have been observed in intracratonic basins which are tectonically inert and within various lithologies which are not necessarily ultramafic [3–5,16–23]. The number of reported sites with natural hydrogen seepages are sixty and growing [24]. Among the many mechanisms known to date, such as, mantle degassing, radiolysis of water due to decay of U, Th, and K, mechanoradicles, decomposition of hydrocarbons, microbial activities [25], Fe^{2+} oxidation remains one of the major sources of natural H_2

* Corresponding author. Universite de Pau et des Pays de l'Adour, E2S UPPA, CNRS, LFCR, Pau, France.
E-mail addresses: kanchana.kularatne@univ-pau.fr (K. Kularatne), pascale.senechal@univ-pau.fr (P. Sénéchal), combaudon.valentine@gmail.com (V. Combaudon), darouich.othmane@univ-pau.fr (O. Darouich), ma.subirana-manzanares@univ-pau.fr (M.A. Subirana), arnaud.proietti@ums-castaing.fr (A. Proietti), caroline.delhaye@u-bordeaux.fr (C. Delhaye), dirk.schaumloeffel@univ-pau.fr (D. Schaumlöffel), olivier.sissmann@ifpen.fr (O. Sissmann), eric.deville@ifpen.fr (E. Deville), hannelore.derluyn@univ-pau.fr (H. Derluyn).

https://doi.org/10.1016/j.ijhydene.2024.06.256
Received 16 December 2023; Received in revised form 3 June 2024; Accepted 17 June 2024
Available online 1 July 2024

generated within the intracratonic basins [26].

No well-developed exploration guide established for natural H_2 exploration [3]. Several proposed guidelines to date are based on geodynamics [1], seismic [1], mineralogical analysis [1] and identification and mapping large scale circular depressions of H_2 seepages [26]. In their work, Lefeuvre and colleagues emphasize that the current knowledge of the hydrogen system is still insufficient to design specific drilling campaigns based solely on one exploration method, but a combination of geophysical, geochemical, and geological data is definitively needed to achieve this goal [3]. In this context, we consider the characterization of source rocks to be crucial, particularly for addressing the fundamental question of how much hydrogen could be generated through the oxidation of Fe^{2+} within the source rock, assuming that H_2 generation occurs exclusively via fluid-rock interactions leading to Fe^{2+} oxidation. Fe^{2+} content in a host rock can be alternatively estimated by wet-chemical methods, Mössbauer spectroscopy, electron energy-loss spectroscopy in a transmission electron microscope (TEM EELS) analysis or using a combination of these techniques with X-ray powder diffraction. The latter are destructive techniques conducted on relatively small samples (a few grams or a nm size thin section of the sample). Therefore, obtaining Fe^{2+} content in a representative sample of a source rock obtained from a geological formation producing natural hydrogen is challenging.

X-ray micro computed tomography (micro-CT) is a non-destructive imaging technique that allows characterization of many materials including rocks [27–31]. Image formation in micro-CT is based on the X-ray linear attenuation coefficient (LAC) of the material which is a function of density and atomic number [27,30]. As a result, this method has been successfully applied to distinguish phases with contrasting densities and/or mineralogical compositions. However, analyzing igneous rocks using micro-CT has been challenging as igneous rocks are composed of multiple minerals with approximately similar LACs [32]. Although these minerals have different chemical compositions, micro-CT lacks chemical information, which is a major limitation to this powerful technique [32,33]. Chemical information can be incorporated into micro-CT by multimodal imaging to characterize various geological materials including reservoir and cap rocks [34–38], metamorphic rocks [39], sediments [40], volcanic tuffs [41], fluid inclusions [42], ores [43], meteorites and planetary materials [29] and granites [32]. These studies demonstrate that the multimodal approaches essentially depend on the sample type, sample size and the size of the heterogeneity needed to be imaged.

In this paper, we propose a multiscale, multimodal imaging workflow tailored to characterize a fractured monzo-diorite obtained from a natural H_2 emitting well in the Precambrian basement in Kansas, USA [44]. The proposed workflow combines 3D micro-CT with 2D chemical information obtained using scanning electron microscopy energy dispersive spectroscopy (SEM EDS), micro-Raman spectroscopy and nano secondary ion mass spectroscopy (NanoSIMS). We identified two Fe^{2+} oxidation reactions leading to natural H_2 generation within the monzo-diorite. We attempted to quantify the potential of H_2 generation per unit rock mass of the monzo-diorite formation assuming that all Fe^{2+} oxidizes while generating H_2. We also extracted the veins to estimate the % of early Fe^{2+} oxidation in the rock. Finally, we discuss the applications and limitations of this method to characterize Fe^{2+}-rich source rocks in the context of natural hydrogen exploration in intracratonic settings.

2. Materials and methods

2.1. Sample description

A core sample of a monzo-diorite obtained from the Precambrian basement of Kansas (DR1-A well), at a depth of 450 m was used in this study. The sample location, geological setting and a detailed mineralogical description of the sample can be found in Combaudon et al [44]. The sample consists of a matrix of orthoclase ($AlK_{0.8}Na_{0.2}Si_3O_8$) and plagioclase ($Al_{1.2}Na_{0.8}Ca_{0.2}Si_{2.8}O_8$), with fayalite ($Fe_{1.8}Mn_{0.1}Mg_{0.1}SiO_4$) + pyroxene ($Fe_{1.6}Mg_{0.5}Mn_{0.1}Si_2O_6$) + amphibole ($Fe_{3.5}Al_{1.9}Ca_{1.7}Mg_{1.1}Na_{0.4}K_{0.2}Si_6O_{22}$) + metal oxides assemblages scattered within this matrix, according to preliminary quantitative SEM EDS performed by Combaudon et al [44]. Preliminary X-ray powder diffraction (XRD) analysis revealed the volume percentages of plagioclase (44 vol%), orthoclase (39 vol.%), mafic minerals (fayalite, pyroxene, amphibole; 10 vol.%), and Fe–Ti oxides (3 vol.%). The XRD pattern is given in SI. 1. All minerals are coarse grained and their sizes are; feldspar (>1 mm–500 mm), pyroxene (~800 μm), amphibole (500 μm-1 mm), fayalite (400 μm-1 mm) and oxides (~500 mm) [44]. Two networks of veins were identified. The first is a network of thicker veins observed only within the fayalite grains and the second is a network of fine veins that cuts across pyroxene, amphibole and then propagates into the feldspar matrix. The FIB-TEM and XANES analysis performed by Combaudon et al [44] indicated that the veins are composed of a mixture of a serpentine + chlorite + micas with $[Fe^{3+}]/\Sigma Fe \sim 0.19$, and interstratified layers of chlorite + smectite and Fe^{3+}-serpentine with $[Fe^{3+}]/\Sigma Fe \sim 0.27$.

2.2. Multiscale, multimodal imaging workflow

The multiscale, multimodal imaging workflow was developed on a cylindrical sample of d = 8.75 mm, l = 17 mm as illustrated in Fig. 1, and elaborated in sections 2.2.1 and 2.2.2. The primary goal is to obtain the volumes of Fe^{2+}-rich phases in the monzo-diorite sample and to estimate the H_2 generation by Fe^{2+} oxidation per unit mass of the rock. The second goal is to obtain the volume and the chemical composition of vein filling minerals to estimate the H_2 that has been already generated as Combaudon et al [44] showed that the veins are filled with Fe^{3+} rich phyllosilicates. The workflow was developed after preliminary SEM EDS and 3D micro-CT analyses conducted on the monzo-diorite sample in the present study and additional characterization given in Combaudon et al [44]. These studies revealed the mineralogical composition, sizes of the minerals and veins which were crucial in determining sample sizes, imaging methods, imaging parameters and resolution.

2.2.1. Phase identification and quantification using 2D chemical analyses and 3D-micro-CT

The LACs of the minerals present in the monzo-diorite sample were calculated based on the NIST XCOM Photon Cross Sections database (www.nist.gov) using "Material Creator", a support tool for the Arion simulator [45] (Fig. 2). The parameters used for this calculation are given in SI. 2. Well-separated curves represent the phases that are distinguishable on the reconstructed micro-CT images, whereas amalgamated curves represent those that appear in approximately similar grey values. Fayalite and Fe–Ti oxides exhibit the highest LAC values when compared to the remaining minerals. Their curves are amalgamated throughout the spectrum of kV values. Plagioclase and serpentine display the lowest LACs and their LACs vary in a similar pattern within the studied range of kV. To summarize, all minerals, with the exception of the latter mineral pairs (fayalite and Fe–Ti; plagioclase and serpentine), can theoretically be differentiated through imaging at energies below 70 kV. We are aware that these theoretical calculations are valid for monochromatic X-ray radiation and that the laboratory measurements, with a polychromatic X-ray source, may yield slightly different results.

To identify the phases in 3-dimensions, first the cylindrical sample of the natural monzo-diorite (Fig. 1a) was imaged at 6 μm voxel size using a Bruker Skyscan 1172 X-Ray microtomograph (DMEX Centre for X-ray Imaging, Pau, France) operated at 70 keV tube voltage with a 0.5 mm Al filter. The whole cylinder was scanned in three batches. Post processing of the image data was done by using the Dragonfly software, version 2022.2.0.1361 for Windows [46]. The 3D visualization revealed that the imaged volume contained a matrix of low-attenuation minerals

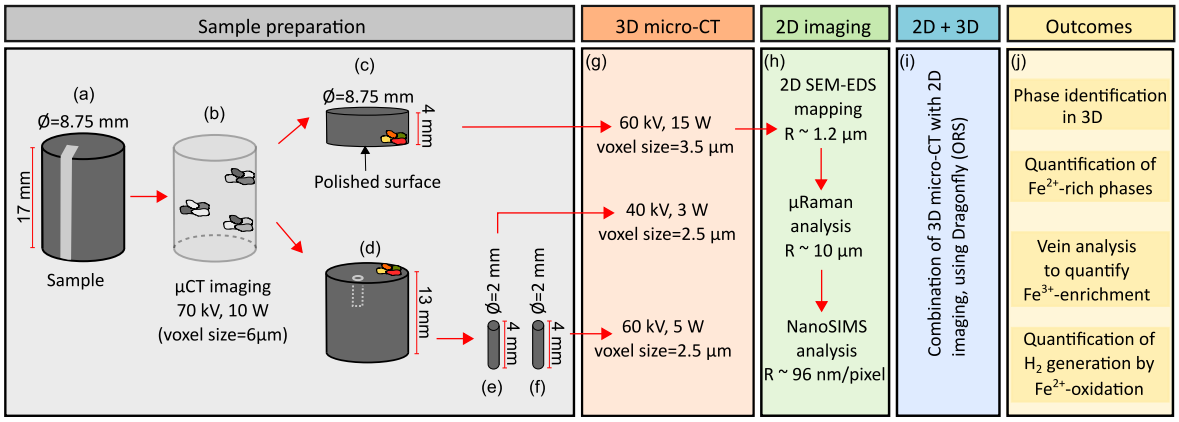

Fig. 1. A sketch showing the multiscale, multimodal imaging workflow developed to study the fractured monzo-diorite, showing the main steps including (a–f) sample preparation, (g) 3D micro-CT imaging, (h) various 2D chemical and mineralogical imaging techniques used to identify phases, (i) combination of 2D chemical and mineralogical information with 3D micro-CT using Dragonfly software, version 2022.2.0.1361 for windows (Comet technologies Canada Inc) to, (j) fully characterize the fractured monzo-diorite sample, non-destructively to quantify potential of H_2 generation by Fe^{2+} oxidation.

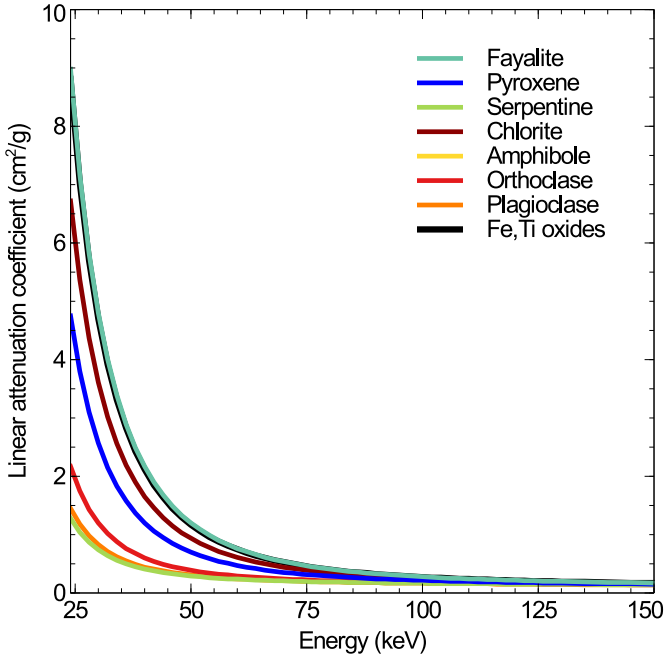

Fig. 2. Variation of calculated linear attenuation coefficients (LACs) of the minerals found in monzo-diorite sample as a function of X-ray energy.

interspersed with clusters of high-attenuation minerals, which is not visible in the thin section scale. X-Ray micro-CT imaging allowed locating one of the typical mineral assemblages within the sample (Fig. 1b). The sample was cut and polished through the chosen assemblage to expose the region of interest (Fig. 1c).

At this point, the identification of minerals present on the exposed surface on micro-CT images is challenging due to the partial volume effect, artefacts, low resolution and also due to the approximately similar or often overlapping grey values of minerals. To improve the image quality, the cylinder with the polished surface (Fig. 1c) was imaged again using a Tescan UniTOM XL Spectral (DMEX Centre for X-ray Imaging, Pau, France). Image acquisition was done at 60 kV and 15 W, with a 1 mm Al filter, to obtain a voxel size of 3.5 µm (Fig. 1g). Although the image quality significantly improved by the latter process, additional chemical information was still necessary to confirm the minerals on the 2D micro-CT slice corresponding to the polished surface of the monzo-diorite sample. This was done by conducting SEM EDS element mapping and micro-Raman spectroscopy (Fig. 1h), as described below.

SEM analysis ((both back scattered electron imaging (BSE) and EDS element mapping) were performed on the polished surface using a MEBFEG JEOL JSM 7100F instrument (Raimond Castaing Microanalysis Centre, at Toulouse, France). 2D elemental distribution of Al, Ca, Fe, K, Mg, Mn, Na, Ni, O, Si, Ti and Zn over the polished surface of the sample was obtained (SI. 3). The instrument was operated at 15 kV, a working distance of 10 mm, and a step size of 1.18 µm. The resulting map is a mosaic of 1969 fields with a magnification of ×500, covering a total surface area of approximately 60 mm^2. The total acquisition time was 19 h. The superposed SEM EDS element maps indicated zones of different mineral phases.

Micro-Raman point analysis was performed to identify the mineralogical composition of the zones with different greyscale values on the micro-CT slice corresponding to the polished sample surface and also to confirm the minerals present in the zones visualized by superposed SEM EDS maps. Micro-Raman spectroscopy was conducted using a Horiba Scientific Xplora Raman spectrometer (Institute des Sciences Moléculaires, University of Bordeaux, France). Point analysis was performed using a 532 nm laser beam, grating 1800 lines/mm, confocal hole aperture 280 µm and slit 100 µm, objective magnification ×50, giving a spatial resolution of ~10 µm and a spectral resolution of ~5 µm, acquisition time 60 s and laser power 10 mW. Peak search-matching was performed using Labspec 6-HORIBA scientific software suit and KnowItAll Raman spectral searching integrated with HORIBA. The location of analysis and Raman spectra of the phases are given in SI. 4.

Once the minerals present on the polished surface of the monzo-diorite sample were corroborated, the phase segmentation was performed on the 3D micro-CT data set by manual thresholding using the Dragonfly software. Prior to segmentation, the noise and artefacts in the data set were filtered using the anisotropic diffusion filter. The segmentation was performed on the micro-CT slice corresponding to the polished surface. The superposed SEM-EDS element distribution maps were used as references to determine the boundary between minerals. The volumes of phases were obtained using the statistical calculation integrated in the same software. Further information about the grey value histograms are given in supplementary information (SI. 5).

Following the same imaging protocol, four additional samples of volumes 511.92 mm^3 (voxel size = 3.5 µm), 944.62 mm^3 (voxel size = 6 µm), 3254.74 mm^3 (voxel size = 10 µm) and 18756.4 mm^3 (voxel size = 30 µm) were imaged to evaluate the representativity of the sample. Further information about this analysis is given in supplementary information (SI. 6).

The mineral volumes, theoretical Fe^{2+} content in the Fe-rich

minerals (fayalite and pyroxene) and the theoretical densities of the minerals were used to calculate the iron content (g) in each mineral. Potential H_2 production per unit mass of the rock ($mol_{(H2)}/kg_{(monzo\text{-}diorite)}$) was then calculated assuming all Fe^{2+} oxidizes according to the stoichiometrically balanced reduction-oxidation (redox) reaction:

$$2Fe^{2+}_{(mineral)} + 2H_2O_{(l)} = 2Fe^{3+}_{(mineral)} + 2OH^-_{(aq)} + H_{2(g)} \quad \text{Eq. 1}$$

2.2.2. Imaging veins in 3D and obtaining the composition of vein-filling materials

Two types of veins were identified as mentioned in section 2.1. The first is a network of thick veins (thickness~18.50 μm) observed only within the fayalite grains and the second is a network of fine veins (thickness~5.50 μm) that cut across pyroxene, amphibole and then propagate into the feldspar matrix. The preliminary micro-CT images showed that these two types of veins are filled with two different vein-filling materials which appear in two different grey values on the micro-CT. Moreover, the preliminary studies showed that these veins could not be extracted successfully when imaged in a single sample due to lack of contrast between the host and the veins. Therefore, we obtained two sub-samples (d~2 mm) cored individually into fayalite and feldspar to perform vein extraction individually. The former was imaged at 60 kV, 5W with 2.5 μm voxel size. The latter was imaged at 40 kV, 3W with 2.5 μm voxel size. Both were imaged using a ZEISS Xradia Versa 510 microtomograph (DMEX Centre for X-ray Imaging, Pau, France). In order to extract the veins, the Segmentation Wizard, a deep learning tool from the Dragonfly software, was used. Twelve slices containing veins were chosen and the veins were painted using the ROI painter. The veins and the rest of the sample were labeled as class 1 and 2 respectively. Then the U net model, one of the deep learning architectures integrated in the Dragonfly software, was chosen as the model generation strategy and this model was trained to identify the predefined veins. The final model was applied for the segmentation of the whole volume to extract the veins in 3D and to obtain the volume fraction of veins.

When polishing the samples, we observed that the densities of the vein-filling minerals and the host-mineral are significantly different, especially in the zones of fractured fayalite, which causes slight topological variations in the polished surface. One of the limitations in SEM EDS element mapping is that it does not correct the beam for topological variations. This could induce an error in the element distribution mapping. Therefore, element distributions in the fractured zones were obtained using NanoSIMS, to avoid the error induced by the topology and to image the veins with sufficiently high spatial resolution. The analysis was conducted using a NanoSIMS 50L CAMECA equipped with a Hyperion™ RF plasma primary oxygen ion source (IPREM, UPPA, France). The oxygen source is necessary for the detection of the elements of Na, Mg, Al, K, Ca, and Fe in this study. The instrument is equipped with seven parallel electron multipliers detectors enabling the simultaneous detection of seven elements during each analysis. We selected representative zones on each type of vein and mapped the distribution of $^{12}C^+$, $^{23}Na^+$, $^{24}Mg^+$, $^{27}Al^+$, $^{39}K^+$, $^{40}Ca^+$, and $^{56}Fe^+$ (SI. 7, 8, 9). The samples had been coated with carbon to improve conductivity and ion yield, and ^{12}C distribution was used to monitor the homogeneity of the sputtering during measurements. Mass calibration was performed with drops of standard solutions (PlasmaCAL, SPC Science, Canada) evaporated on silicon wafers, and interferences were eliminated by optimizing the mass resolution. The sample was coated with 5 nm of gold layer to improve conductivity and ion yield using a 108-auto sputter coater (Cressington, UK). Images covering 50 μm × 50 μm areas were pre-sputtered with an O^- current of 580 pA and then collected with a current of 5 pA, with 512 × 512 pixels and 10 m s of dwell time per pixel, and a spatial resolution of approximately 100–150 nm. Images were then fused to obtain mosaics when necessary and processed using the software WinImage (Cameca).

3. Results

3.1. 2D and 3D phase identification and quantification

The 3D micro-CT volume of the sample and the 2D micro-CT slice corresponding to the polished surface of the monzo-diorite sample are given in Fig. 3a and b, respectively. The histogram of grey values of the 2D micro-CT slice in Fig. 3a is given in SI.5. The SEM BSE image of the polished surface imaged at 1.18 μm resolution is given in Fig. 3c. On this image, the major mineral phases previously identified [44] are also marked. Fig. 3d shows an image of superposed SEM EDS element distribution maps of Fe, Mg, Ca and Al acquired on the polished surface of the monzo-diorite sample. Similar to Fig. 3c, the major mineral phases identified using micro-Raman point analysis are also marked. Micro-Raman spectra are given in SI.4. According to this identification, it can be seen that the majority of the sample consists of orthoclase and plagioclase indicated by the lowest greyscale values on Fig. 3a and b. Oxides are present as few small grains that correspond to the highest greyscale values (Fig. 3a and b). Fayalite is highly fractured. Fine veins within the feldspar could be clearly observed on Fig. 3c and d (higher resolution SEM BSE images highlighting the veins are provided in SI. 7). The seven major mineral phases can be easily distinguished on the superposed SEM EDS element distribution map (Fig. 3d). The individual SEM EDS element maps showing the distribution of Na, K, Fe, Ti, Ca, and Mg are given in supplementary information (SI.3).

Five phases were segmented on the 2D micro-CT slice using manual thresholding (Fig. 3e). These phases are (1) oxides (greyscales 17,000–65508), (2) fayalite (greyscales 13,500–17000), (3) pyroxene (greyscales 10,100–13500), (4) amphibole (greyscales 8675–10100) and (5) feldspars (greyscales 3474–8675). The veins within fayalite are composed of a mixture of serpentine and chlorite, however they were thresholded together with pyroxene due to their similar greyscale range restricting the segmentation possibility. 3D visualization of phases (without feldspar) is given in Fig. 3f. The average volume percentages (vol%) of minerals are; feldspar (81.51 ± 1.26 vol%), pyroxene (11.38 ± 0.77 vol %), amphibole (vol. 5.31 ± 0.36 %), fayalite (1.30 ± 0.09 vol %), and oxides (0.5 ± 0.03 vol %) (see also SI.6).

3.2. H_2 generation per unit mass of source rock

Two reactions were identified as potential Fe^{2+} oxidation reactions: (1) pyroxene transformation into amphibole, (2) fayalite transformation into a mixture of serpentine and chlorite that precipitate within the veins. The chemical formula of pyroxene (ferrosillite) and fayalite used for the calculation are $Fe_{1.6}Mg_{0.5}Mn_{0.1}Si_2O_6$ and $Fe_{1.8}Mn_{0.1}Mg_{0.1}SiO_4$, with densities 3.95 g/cm^3 and 4.39 g/cm^3 respectively (SI.10). The theoretical Fe^{2+} content in pyroxene and fayalite with the chemical formula above are 0.43 g/mol and 0.50 g/mol respectively. The average volume percentages of pyroxene and fayalite obtained from X-ray micro-CT are 1.3 vol% and 11.38 vol%. The volume of full sample, pyroxene and fayalite was taken as 100 mm^3, 1.3 mm^3 and 11.38 mm^3. Density of the rock is 2.8 g/cm^3. The calculated Fe^{2+} content in pyroxene and fayalite in 100 mm^3 volume of the rock are 35.2 mg and 2.9 mg, respectively. Assuming that all iron in both minerals are divalent (Fe^{2+}) and that they oxidize completely, generating H_2 (Eq. (1)), then pyroxene and fayalite oxidation would generate 615.03 ± 8.61 mol (H_2)/ton (source rock) and 92.90 ± 27.26 mol (H_2)/ton (source rock) respectively. The upper limit of H_2 generation of the whole rock would be 707.93 ± 49.18 mol (H_2)/ton (source rock).

3.3. Vein extraction in 3D and the composition of the vein-filling minerals

The veins within fayalite account for 3.83 ± 0.41 vol% of its volume and 0.05 ± 0.39 vol% of the full sample volume, while those within feldspar constitute 1.20 ± 0.16 vol% of its volume and 0.98 ± 0.15 vol% of the full sample volume. Fig. 4a displays an imaged volume of fayalite

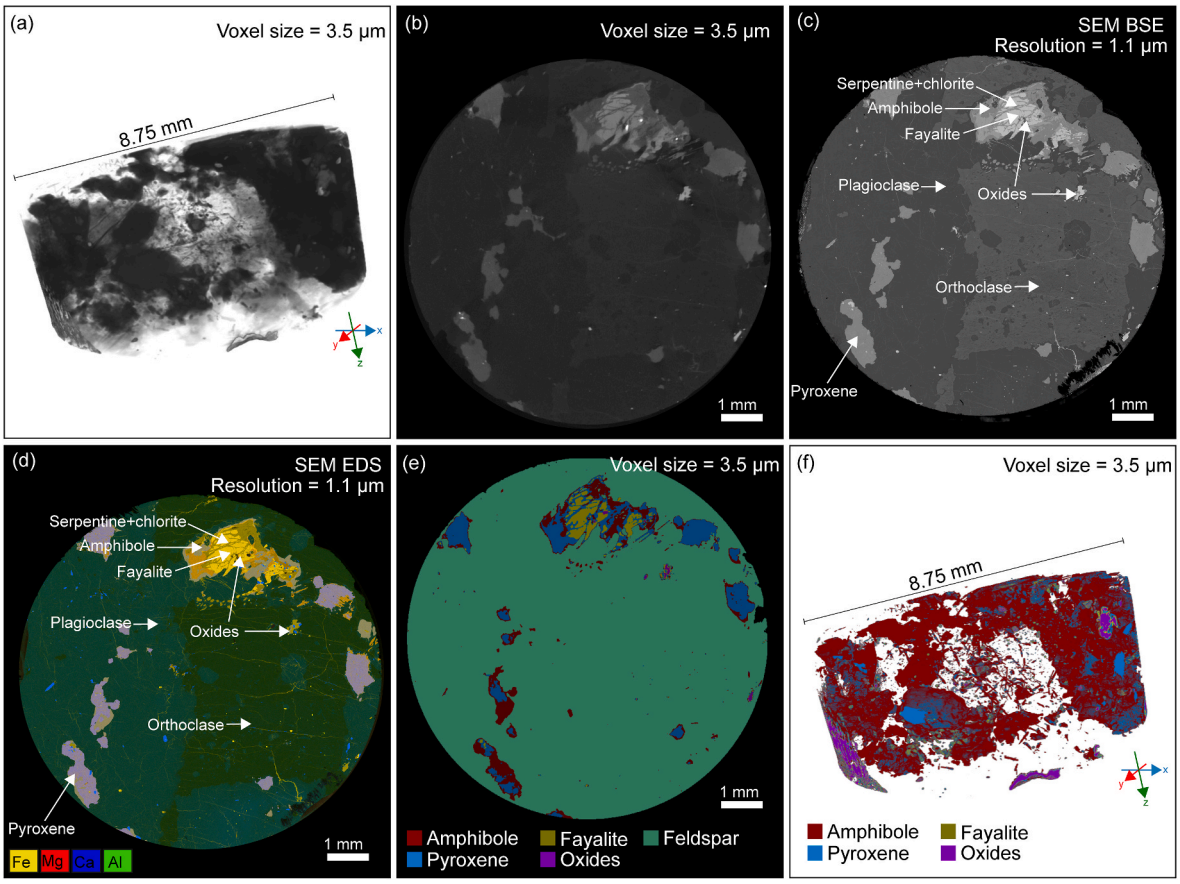

Fig. 3. Identification of major phases in the monzo-diorite sample in 3-dimensions using the developed multimodal workflow (a) 3D micro-CT volume of the sample imaged at voxel size of 3.5 µm (b) 2D micro-CT slice corresponding to the polished surface of the sample (c) Scanning electron microscopy imaging performed using back scattered electron diffraction mode (SEM BSE), and (d) Superposed SEM EDS element distribution maps of Fe, Mg, Ca, and Al collected on the polished sample surface showing the seven mineral phases distinguished based on their chemical composition reflected by different colors (e) 2D micro-CT slice corresponding to the polished surface showing the five phases segmented using Dragonfly (f) 3D visualization of five phases identified in the monzo-diorite sample, feldspar (>80 vol.%) is not shown in the figure for clarity. (For interpretation of the references to color in this figure legend, the reader is referred to the Web version of this article.)

grain containing veins, with Fig. 4b showing the interconnected mesh-like structure of extracted veins. Veins range in thickness from 5.00 µm to 63.00 µm with an average of ~18.50 µm. Similarly, Fig. 4d and e illustrate the imaged volume of feldspar with veins and extracted veins showing parallel planer arrangement, respectively. The veins exhibit thicknesses ranging from 3.00 µm to 11.00 µm, with an average thickness of approximately 5.50 µm. Fig. 4c illustrates the enrichment of veins within fayalite in Fe, with small amounts of Al and Mg, and traces of Na and Ca, but absence of K. In contrast, Fig. 4f depicts the enrichment of veins within feldspar in Mg and Al, with Fe and Ca present in trace amounts, and no Na or K detected.

The veins formed within fayalite show a close similarity to the composition of host fayalite. Fig. 4c shows that both veins and fayalite are poor in Na, K, Al, and Ca, but rich in Fe. However, the veins contain less Mg than fayalite (note that fayalite contains low Mg content in the structure as the fayalite in the current study has a chemical composition of ~Fa90). On the contrary, the veins formed within feldspar do not show a close compositional relationship to pyroxene and amphibole. As shown in Fig. 4f the veins within feldspar are depleted in Na, Ca, but enriched in Mg and Fe compared to the host feldspar. Both veins and feldspar are depleted in K.

3.4. Veins and their contribution to hydrogen generation

The veins within fayalite provide direct evidence for H_2 already generated within the monzo-diorite [44]. Combaudon et al [44] details that the veins within fayalite consist of a central vein with a mixture of serpentine + chlorite + micas with $[Fe^{3+}]/\Sigma Fe$ value of 0.19 and a border vein composed of interstratified Fe^{3+} serpentine + smectite and then a Fe^{3+} serpentine in direct contact with the fayalite, each consisting of a $[Fe^{3+}]/\Sigma Fe$ value of 0.27. The veins in feldspar are also rich in Fe^{3+} with a $[Fe^{3+}]/\Sigma Fe$ value of 0.45, however, they might not be linked to iron oxidation but rather to the initial magmatic liquid composition, thus do not contribute to H_2 generation [44]. We attempted to calculate the H_2 already generated within the rock via fayalite alteration. For simplicity of modeling, we assumed that the veins within fayalite are composed of Fe^{3+}-rich serpentine ($Fe_3Si_2O_5(OH)_4$) with $[Fe^{3+}]/\Sigma Fe$ value of 0.27. The considered volume percentage of veins within the rock is 0.05 ± 0.39 vol%. Volume and the density of the rock is 100 mm^3 and 2.8 g/cm^3 respectively. The molar mass and density of the Fe^{3+}-rich serpentine is 371.7 g/mol and 3.35 g/cm3 respectively. The calculated Fe^{3+} content in 100 mm^3 volume of the rock is 1.35 ± 0.24 µmols. Assuming that all iron in both minerals are divalent (Fe^{2+}) and that they oxidize completely, generating H_2 (Eq. (1)), the fayalite alteration in the rock has generated 2.19 ± 0.39 mol (H_2)/ton (source rock).

4. Discussion

4.1. Advantages and limitations of the proposed workflow

The proposed workflow offers an imaging approach to estimate the upper limit of H_2 generation by Fe^{2+} oxidation in Fe-rich lithologies. This method is based on the major assumption that all Fe^{2+} in the source rock oxidizes generating H_2 according to Equation (1), which offers a

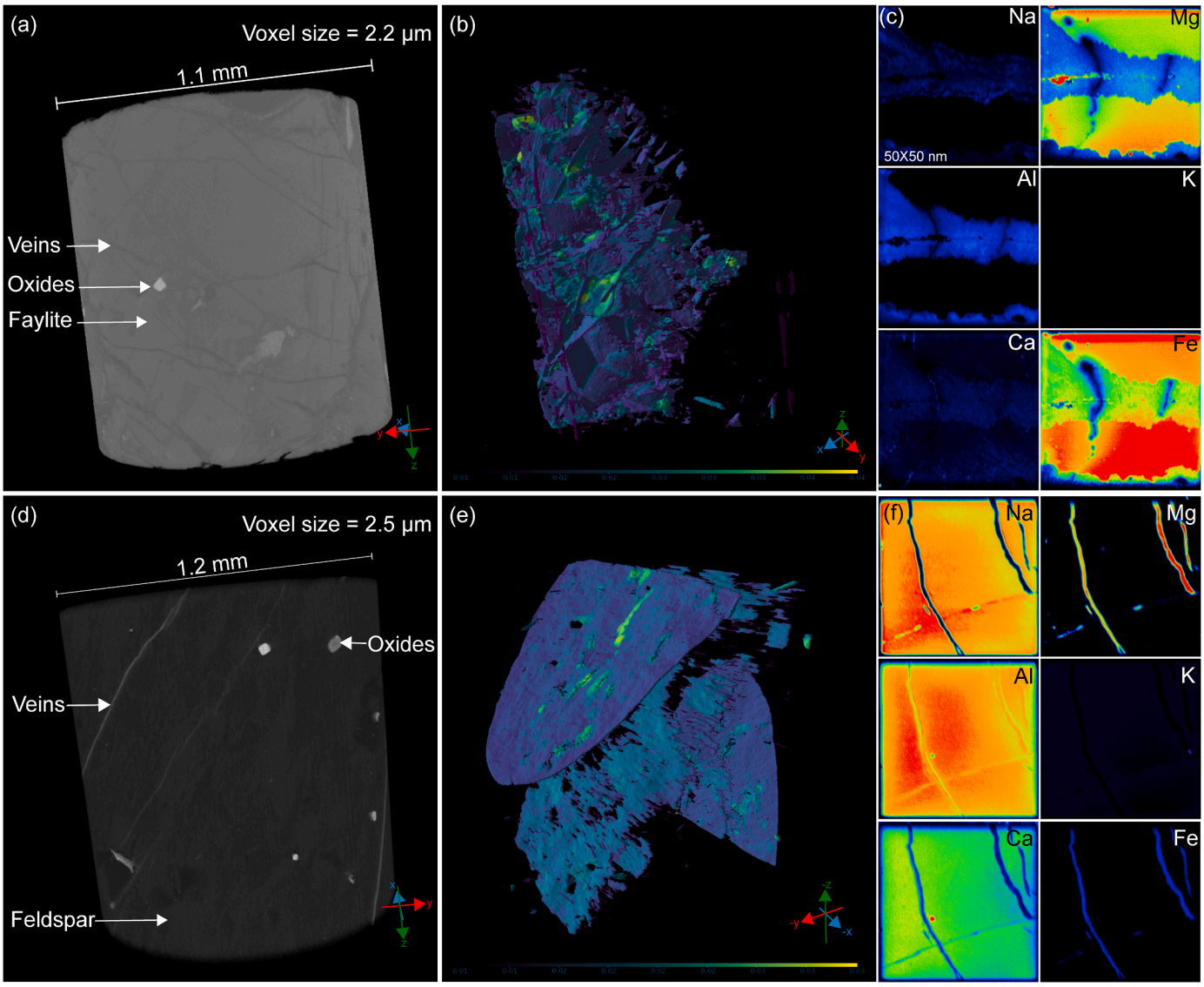

Fig. 4. Veins in the monzo-diorite sample (a) 3D micro-CT volume of the sub sample cored into fayalite (b) veins within fayalite visualized in 3D, the yellow areas are the thickest (~40 μm) and the purple are the thinnest (~10 μm) (c) Composition of veins in a 50 μm × 50 μm area within fayalite obtained using NanoSIMS analysis, where red represents the highest concentration and black represent the lowest concentrations, for all elements (d) 3D micro-CT volume of the sub sample cored into feldspar (e) veins contained within feldspar visualized in 3D, the yellow areas are the thickest (~30 μm) and the purple are the thinnest (~10 μm) (f) Composition of veins in a 50 μm × 50 μm area within feldspar, obtained using NanoSIMS analysis, where red represents the highest concentration and black represent the lowest concentrations, for all elements. (For interpretation of the references to color in this figure legend, the reader is referred to the Web version of this article.)

simple stoichiometric ratio between Fe^{2+} and H_2 which is 2:1. Therefore, accurate quantification of Fe^{2+} in the source rock ensures accurate amount of H_2 generated via Fe^{2+} oxidation. Fe^{2+} content in a rock sample can be determined either by using traditional wet chemical methods such as Mohr's salt method [47], 1,10-Phenanthroline Method [48], Wilson's method [49,50], or modern spectroscopic methods including Mössbauer Spectroscopy, electron energy-loss spectroscopy in a transmission electron microscope (TEM EELS), X-ray absorption near-edge structure (XANES) spectroscopy, inductively coupled plasma optical emission spectroscopy (ICP-OES) and atomic absorption spectroscopy (AAS). While the wet chemical methods, ICP-OES, AAS, and Mössbauer Spectroscopy involve complete sample destruction, TEM EELS and XANES are often performed on nanometer-sized zones on a 2D thin section. Given the inherent heterogeneity of natural rock formations, ensuring sample representativity is paramount for accurate Fe^{2+} determination. To obtain representative Fe^{2+} value, the above-mentioned methods often necessitate the collection of small, multiple samples from a target formation, a process both time-consuming and costly, ultimately resulting in sample destruction. In contrast, our proposed methodology offers the capacity to analyze larger rock volumes, such as 1-m long drill cores, leveraging advanced tomographic instrument.

In addition to imaging larger volumes, choosing representative volumes is crucial for the proposed workflow. The current workflow is developed using a sample volume of 240.53 mm^3 (Fig. 1). A volume of 217.50 mm^3 was considered for the micro-CT data treatment. However, four additional samples were used to evaluate the representativity of the sample volume chosen for the analysis (SI.6). The larger sample volumes such as 18756.4 mm^3 images at voxel size = 30 μm, and 3254.74 mm^3 imaged at voxel size = 10 μm were used to obtained the volume fraction between the matrix and the mineral assemblages. Then the volume fractions between the minerals within the assemblages were imaged at higher resolutions over volumes 944.62 mm^3 imaged at voxel size = 6 μm, and 511.92 mm^3 imaged at voxel size = 3.5 μm. The volumes obtained from the four larger samples are seemingly coherent compared to the volumes obtained from the small sample shown in Fig. 1, regardless

of imaging at larger voxel sizes. Therefore, it is important to emphasize that the sample used for the imaging must be sufficiently large and representative for the mineral volumes of interest, whether it is on the scale of the mineral cluster fayalite-pyroxene-amphibole-oxides only, or on the scale of all minerals including the feldspar matrix.

The current method utilizes SEM EDS, micro-Raman analysis and NanoSIMS to obtain element distribution and to confirm the minerals on the 2D section of the sample, however, these techniques are not mandatory. Users may employ any appropriate technique to identify phases within the greyscale micro-CT images. Consequently, a streamlined workflow could integrate 2D data obtained from petrographic microscopy of thin sections with 3D micro-CT imaging. This approach is viable provided that the petrographic microscopy can sufficiently identify the phases observed in the greyscale micro-CT images.

The developed method is capable of identifying five out of seven phases present in the studied sample in three-dimension, while distinguishing minerals with similar grey scale ranges remain unresolved (Fig. 3). For example, plagioclase, orthoclase and the veins within them could not be distinguished due to overlapping greyscale ranges between 3474 and 8675 (Fig. 3a and b). Similarly, pyroxene and the vein-filling mineral (mixture of serpentine and chlorite) found within the veins in fayalite, could not distinguished due to their overlapping greyscale ranges between 10,100 and 13500 (Fig. 3a and b). The similar grey scale values of plagioclase and orthoclase arise due to their similar LACs, which is a result of approximately similar molecular weights (238.44 mol^{-1} and 275.11 mol^{-1}), and approximately similar densities (2.62 gcm^{-3} and 2.56 gcm^{-3}). Moreover, pyroxene and the vein-filling phase have approximately similar molecular weights (631.4 mol^{-1} and 555.8 mol^{-1}) and densities (3.95 gcm^{-3} and 2.6 gcm^{-3}) (SI.10) resulting in approximately similar LACs. This induced a slight overestimation of the volume of pyroxene. Similar problematics have been encountered in phase segmentation in a granite containing quartz, feldspar and ferromagnesian phases, reported by Boone and colleagues [32], using a laboratory micro-CT based multimodal imaging.

Phase segmentation can be affected by unavoidable artefacts such as the metal streak artefacts that are commonly found associated with Fe, Ti-oxides. These artefacts are visible as a rim of white voxels on the 2D micro-CT slices. These white voxels were assigned to fayalite, in order to avoid a significant under-segmentation of fayalite.

In certain studies, 2D chemical information obtained by SEM-EDS element maps are propagated over the 3D micro-CT volume by 2D-3D registration [35,39]. However, due to the large number of phases with overlapping grey-scale values, 2D-3D registration of SEM EDS maps was not conducted. Moreover, phase segmentation in igneous rocks with complex structures and textures needs human intervention in order to conduct a reliable segmentation as automatic thresholding or Machine learning based segmentation could cause errors in handling complex igneous structures and textures, as also observed by Boone et al [32].

One of the major challenges associated with the veins in this sample is the presence of two networks of veins within two types of matrices. As a result, the veins cannot be extracted by imaging a single subsample that contains both type of veins. Imaging a single subsample at an energy suitable for the whole subsample, resulted in a low-contrast between the veins and their respective host-minerals. The attempt to use machine learning based segmentation on the whole sample was not successful as the vein distribution is highly heterogeneous. However, we have shown that this problem can be overcome by subsampling into two vein networks (located within feldspar and within fayalite) separately and by imaging them separately at suitable energies. This allows obtaining quality datasets of the two types of veins.

4.2. Quantification of natural H_2 generation in monzo-diorite from the precambrian basement in Kansas, USA

Our estimation shows that the studied sample could potentially generate 707.93 ± 9.18 mol (H_2)/ton (source rock), by complete oxidation of Fe^{2+} via (1) pyroxene transformation into amphibole, (2) fayalite transformation into a mixture of serpentine and chlorite that precipitate within the veins. Each reaction separately generates 615.03 ± 8.61 mol (H_2)/ton (source rock) and 92.90 ± 27.26 mol (H_2)/ton (source rock), respectively. The alteration of fayalite into the Fe^{3+}-rich mineral assemblage within the veins has generated 2.19 ± 0.39 mol (H_2)/ton (source rock). The total Fe^{2+} content in the monzo-diorite is 7.90 wt% as calculated based on the mineral volumes obtained from 3D micro-CT imaging and the theoretical Fe^{2+} content of minerals. This value is in the same order of magnitude as in banded iron formations (BIF) which contains ~20–40 wt% of Fe (tot) [21]. A BIF with 11 wt% of Fe^{2+} can theoretically generate 1000 mol (H_2)/ton (source rock), by the oxidation of Fe^{2+} in magnetite into Fe^{3+} in goethite and hematite mixture [21], which is similar to the estimated H_2 generation of Kansas rocks in this study.

4.3. Implications to natural H_2 exploration

The proposed method contributes to one of the major tasks in the exciting natural H_2 exploration, which is the global estimation of the potential of H_2 production per unit mass of the source rock, where H_2 is produced by fluid-rock interactions. The rocks that generate H_2 through the redox reaction between Fe^{2+} and water are grouped into H2_GR1 (Basic and ultrabasic rocks) and H2_GR2 (Iron-bearing rocks) according to the recent work by Lévy and co-workers [51]. H2_GR1and H2_GR2 encompasses peridotite, gabbro, basalt, ophiolite massifs, granites, Fe-rich sedimentary formations and banded iron formations (BIF) [50,52–81]. Within these lithologies, several Fe^{2+} oxidation pathways leading to H_2 generation in the intracratonic settings have been documented.

(1) Low temperature serpentinization [1,9,10,82–84]:

$$\text{Olivine} + H_2O \rightarrow \text{Serpentine} \pm \text{Brucite} \pm \text{Magnetite} + H_{2(g)} \quad \text{Eq. 2}$$

$$\text{Olivine} + \text{pyroxene} + H_2O \rightarrow \text{Serpentine} + \text{Magnetite} + H_{2(g)} \quad \text{Eq. 3}$$

(2) Fayalite decomposition in late stage crystallization of basic magma [85]:

$$3Fe_2SiO_{4(\text{fayalite})} + 2H_2O_{(l)} \rightarrow 2Fe_3O_{4(\text{magnetite})} + 3SiO_{2(\text{quartz})} + 2H_{2(g)} \quad \text{Eq. 4}$$

(3) Siderite alteration [86,87]:

$$3FeCO_{3(\text{siderite})} + H_2O_{(l)} \leftrightarrow Fe_3O_{4(\text{magnetite})} + 3CO_{2(g)} + H_{2(g)} \quad \text{Eq. 5}$$

(4) Magnetite alteration [85]:

$$2Fe_3O_{4(\text{magnetite})} + H_2O_{(l)} \rightarrow 3Fe_2O_{3(\text{hematite})} + H_{2(g)} \quad \text{Eq. 6}$$

(5) Pyritization [85]:

$$Fe_2O_{3(\text{hematite})} + 4H_2S_{(g)} \rightarrow 2FeS_{2(\text{pyrite})} + 3H_2O_{(l)} + H_{2(g)} \quad \text{Eq. 7}$$

$$Fe_3O_{4(\text{magnetite})} + 6H_2S_{(g)} \rightarrow 3FeS_{2(\text{pyrite})} + 4H_2O_{(l)} + 2H_{2(g)} \quad \text{Eq. 8}$$

(6) Alterations in granites [25,88–90]

$$\text{Biotite} + H_2O \rightarrow Fe_2^{3+}O_{3(\text{goethite/hematite})} + H_{2(g)} \quad \text{Eq. 9}$$

$$\text{Biotite} + H_2O \rightarrow Fe_3O_{4(\text{magnetite})} + H_{2(g)} \quad \text{Eq. 10}$$

$$\text{Arfvedsonite} + H_2O \rightarrow \text{aegirine} + H_{2(g)} \quad \text{Eq. 11}$$

(7) Alterations in banded iron formations (BIF) [21,91]:

$$2Fe^{2+}O_{(\text{silicate})} + H_2O_{(g)} \rightarrow Fe^{3+}O_{3(\text{goethite})} + H_{2(g)} \quad \text{Eq. 12}$$

$$2Fe^{2+}O_{(\text{magnetite})} + H_2O_{(g)} \rightarrow Fe_2^{3+}O_{3(\text{goethite/hematite})} + H_{2(g)} \quad \text{Eq. 13}$$

(8) Alterations in monzo-diorite (This study [44]):

$$\text{Fayalite} + H_2O \rightarrow \text{serpentine} + \text{chlorite} + H_{2(g)} \quad \text{Eq. 14}$$

$$\text{Pyroxene} + H_2O \rightarrow \text{amphibole} + H_{2(g)} \quad \text{Eq. 15}$$

The proposed workflow can be applied to model the upper limit of H_2 generation via most of the reported Fe^{2+} oxidation reactions except for the reactions involving multiple minerals with similar linear attenuation coefficients at the measured energy. We calculated the theoretical linear attenuation coefficients (LACs) of the minerals involved in the eight reaction types given above (Eqs. (2)–(15)) The parameters used for the calculation and the variation of LAC as a function of energy are given in SI. 2 , respectively. The calculations indicate that the following mineral pairs exhibit similar behavior of LAC as a function of X-ray energy: brucite-serpentine (Eq. (2)), magnetite-hematite (Eq. (6)), aegirine-biotite (Eqs. (9)–(11)), biotite-arfvedsonite (Eqs. (9)–(11)), pyroxene-amphibole (Eq. (15)).

The LACs plotted in SI. 11 were calculated assuming that the entire sample consists of the mineral involved in the reactions given in Eqs. (2)–(15). However, the rocks could contain other minerals that might not participate in the Fe^{2+} oxidation. When applying the proposed workflow, it is important to consider the LACs of all minerals present in the sample in order to understand whether there are other minerals which could interfere with the LAC of the Fe^{2+}-rich mineral/s of interest. A more detailed assessment of the true LACs could involve simulating the X-ray micro-CT scan prior to performing the experiment, e.g., using the Arion software package [45]. To simulate a realistic X-ray micro-CT image, this program utilizes the density and the chemical formula of the phase together with the source, detector and operating parameters of the micro-CT instrument [45,92,93]. This method can reconstruct realistic greyscale images that are comparable to the actual micro-CT images acquired with the equipment used in this study [93]. However, the current study conducted only a general assessment of grey values of the phases independent of the instrument.

However, two phases with similar greyscale values could also be distinguished by using several other techniques yet out of the scope of the current study. For example, the dual-energy CT technique (DECT) [94] using either synchrotron monochromatic X-ray beam [95] or recently developed laboratory-based method [92] allows distinguishing phases with similar LACs. Moreover, with the developments in laboratory based spectral tomography techniques (sp-CT), modeling alterations in rocks would no longer be limited by the minerals' LACs, as sp-CT allows phase identification based on the chemical composition of the material [96,97].

Most natural rocks are heterogeneous. These heterogeneities could vary from nano-meter (nm) scale to kilometer (km) scale. Therefore, when modeling the H_2 generation potential of a certain lithology it is important to have a sound knowledge about the heterogeneities in the considered rock formation and to obtain the most representative samples for imaging.

5. Conclusions

The proposed workflow provides a novel approach to estimate the upper limit of hydrogen (H_2) generation via Fe^{2+} oxidation in Fe-rich lithologies by correlative imaging of source rock. By merging 2D chemical and mineralogical information with 3D volumes obtained by X-ray computed tomography, this method allows the analysis of larger rock volumes, including 1 m long drill cores. This approach addresses the limitations of traditional wet chemical and modern spectroscopic methods, which are often destructive and that require small and potentially unrepresentative samples. Applying the developed workflow, a monzo-diorite in Precambrian basement of Kansas, USA was analyzed. This work has led to following conclusions.

1. Monzo-diorite in the Precambrian basement of Kansas, USA contains fayalite and pyroxene, two Fe^{2+}-rich minerals that could generate H_2 via the redox reaction with water.
2. Assuming that all Fe^{2+} contained in these two minerals oxidizes generating H_2, this formation is capable of generating 707.93 ± 49.18 mol (H_2)/ton (source rock), which is in the same order of magnitude as that of BIF previously reported. This value sets the upper limit to the H_2 generation in monzo-diorite in Kansas, USA.
3. The veins within fayalite represent Fe^{2+} that has been already oxidized generating 2.19 ± 0.39 mol (H_2)/ton (source rock).
4. The applicability of this workflow relies upon having mineral assemblages with distinguishable grey scale values when imaged with micro-CT. This study shows that most of the reported Fe^{2+} oxidation reactions leading to natural H_2 generation can be modeled using the proposed method, except those involved with minerals with similar LACs.
5. However, challenges remain in phase segmentation due to overlapping greyscale values of certain minerals, necessitating further refinement through dual-energy CT or spectral-CT techniques. Addressing these challenges will enhance the accuracy of mineral identification and volume estimation in heterogeneous rock formations.
6. Overall, the proposed workflow represents a significant advancement in natural H₂ exploration, offering a comprehensive, efficient, and non-destructive method for analyzing large rock volumes and enhancing our understanding of natural hydrogen generation in intracratonic settings.

CRediT authorship contribution statement

Kanchana Kularatne: Conceptualization, Data curation, Formal analysis, Investigation, Methodology, Software, Validation, Visualization, Writing – original draft, Writing – review & editing. **Pascale Sénéchal:** Conceptualization, Formal analysis, Investigation, Methodology, Software, Writing – original draft. **Valentine Combaudon:** Conceptualization, Investigation, Methodology, Resources, Validation, Writing – original draft. **Othmane Darouich:** Data curation, Formal analysis, Investigation, Methodology, Software. **Maria Angels Subirana:** Data curation, Formal analysis, Investigation, Methodology, Writing – original draft. **Arnaud Proietti:** Data curation, Formal analysis, Methodology, Writing – original draft. **Caroline Delhaye:** Data curation, Formal analysis, Methodology, Writing – original draft. **Dirk Schaumlöffel:** Data curation, Formal analysis, Methodology, Project administration, Supervision, Writing – original draft. **Olivier Sissmann:** Conceptualization, Funding acquisition, Resources, Supervision, Writing – review & editing, Methodology. **Eric Deville:** Conceptualization, Funding acquisition, Methodology, Project administration, Supervision. **Hannelore Derluyn:** Conceptualization, Funding acquisition, Project administration, Supervision, Writing – review & editing.

Declaration of competing interest

The authors declare that they have no known competing financial interests or personal relationships that could have appeared to influence the work reported in this paper.

Acknowledgements

This research was funded under the framework of the E2S UPPA hub Newpores supported by the Nouvelle-Aquitaine Region and by the "France 2030" Investment Programme managed by the French National Research Agency (ANR-16-IDEX-0002). H. Derluyn acknowledges the support from the European Research Council (ERC) under the European Union's Horizon 2020 research and innovation programme (grant agreement No 850853)".

Appendix A. Supplementary data

Supplementary data to this article can be found online at https://doi.org/10.1016/j.ijhydene.2024.06.256.

References

[1] Dugamin E, Truche L, Donzé FV. Natural hydrogen exploration guide, vol. 1. ISRN Geonum-NST; 2019. p. 16.
[2] Gaucher EC. New perspectives in the industrial exploration for native hydrogen. Elements 2020;16(1):8–9.
[3] Lefeuvre N, Truche L, Donzé FV, Ducoux M, Barré G, Fakoury RA, Calassou S, Gaucher EC. Native H2 exploration in the western pyrenean foothills. G-cubed 2021;22(8):1–20.
[4] Truche L, McCollom TM, Martinez I. Hydrogen and abiotic hydrocarbons: molecules that change the world. Elements: Int. Magazine of Mineral., Geochem., and Petrol. 2020;16(1):13–8.
[5] Truche L, Donzé FV, Dusséaux C, Lefeuvre N, Brunet F, Malvoisin B. The quest for native hydrogen: new directions for exploration (À la recherché de l'hydrogène natif: de nouvelles orientations pour l'exploration). Géologues géosciences et société 2022;213:68–73.
[6] Malvoisin B, Brunet F, Carlut J, Rouméjon S, Cannat M. Serpentinization of oceanic peridotites: 2. Kinetics and processes of San Carlos olivine hydrothermal alteration. J Geophys Res Solid Earth 2012;117(4):1–13.
[7] Marcaillou C, Muñoz M, Vidal O, Parra T, Harfouche M. Mineralogical evidence for H2 degassing during serpentinization at 300°C/300bar. Earth Planet Sci Lett 2011;303(3–4):281–90.
[8] Mayhew LE, Ellison ET, McCollom TM, Trainor TP, Templeton AS. Hydrogen generation from low-temperature water-rock reactions. Nat Geosci 2013;6(6):478–84.
[9] McCollom TM, Bach W. Thermodynamic constraints on hydrogen generation during serpentinization of ultramafic rocks. Geochem Cosmochim Acta 2009;73(3):856–75.
[10] McCollom TM, Seewald JS. Serpentinites, hydrogen, and life. Elements 2013;9(2):129–34.
[11] Etiope G, Schoell M. Abiotic gas: atypical, but not rare. Elements 2014;10(4):291–6.
[12] Fu Q, Sherwood Lollar B, Horita J, Lacrampe-Couloume G, Seyfried WE. Abiotic formation of hydrocarbons under hydrothermal conditions: constraints from chemical and isotope data. Geochem Cosmochim Acta 2007;71(8):1982–98.
[13] McCollom TM. Laboratory simulations of abiotic hydrocarbon formation in earth's deep subsurface. Rev Mineral Geochem 2013;75:467–94.
[14] McCollom TM, Lollar BS, Lacrampe-Couloume G, Seewald JS. The influence of carbon source on abiotic organic synthesis and carbon isotope fractionation under hydrothermal conditions. Geochem Cosmochim Acta 2010;74(9):2717–40.
[15] Proskurowski G, Lilley MD, Seewald JS, Früh-Green GL, Olson EJ, Lupton JE, Sylva SP, Kelley DS. Abiogenic hydrocarbon production at lost city hydrothermal field. Science 2008;319(5863):604–7.
[16] Larin AV. Deblocking effect of carbonates and hydrogen carbonates in the alkali form zeolites with narrow pores. Microporous Mesoporous Mater 2014;200:35–45.
[17] Zgonnik V, Beaumont V, Deville E, Larin N, Pillot D, Farrell KM. Evidence for natural molecular hydrogen seepage associated with Carolina bays (surficial, ovoid depressions on the Atlantic Coastal Plain, Province of the USA). Prog Earth Planet Sci 2015;2:1–15.
[18] Guélard J, Beaumont V, Rouchon V, Guyot F, Pillot D, Jézéquel D, Ader M, Newell KD, Deville E. Natural H2 in Kansas: deep or shallow origin? G-cubed 2017;18(5):1841–65.
[19] Prinzhofer A, Moretti I, Françolin J, Pacheco C, D'Agostino A, Werly J, Rupin F. Natural hydrogen continuous emission from sedimentary basins: the example of a Brazilian H2 -emitting structure. Int J Hydrogen Energy 2019;44(12):5676–85.
[20] Combaudon V, Moretti I, Kleine BI, Stefánsson A. Hydrogen emissions from hydrothermal fields in Iceland and comparison with the Mid-Atlantic Ridge. Int J Hydrogen Energy 2022;47(18):10217–27.
[21] Geymond U, Ramanaidou E, Lévy D, Ouaya A, Moretti I. Can weathering of banded iron formations generate natural hydrogen? Evidence from Australia, Brazil and South Africa. Minerals 2022;12(2):163.
[22] Maiga O, Deville E, Laval J, Prinzhofer A, Diallo AB. Characterization of the spontaneously recharging natural hydrogen reservoirs of Bourakebougou in Mali. Sci Rep 2023;13(1):11876.
[23] Loiseau K, Aubourg C, Petit V, Bordes S, Lefeuvre N, Thomas E, Moretti I. Hydrogen generation and heterogeneity of the serpentinization process at all scales: Turon de Técouère lherzolite case study, Pyrenees (France). Geoenergy 2024;2(1). geoenergy2023-024.
[24] McMahon CJ, Roberts JJ, Johnson G, Edlmann K, Flude S, Shipton ZK. Natural hydrogen seeps as analogues to inform monitoring of engineered geological hydrogen storage. 2023.
[25] Truche L, Bourdelle F, Salvi S, Lefeuvre N, Zug A, Lloret E. Hydrogen generation during hydrothermal alteration of peralkaline granite. Geochem Cosmochim Acta 2021;308:42–59.
[26] Moretti I, Brouilly E, Loiseau K, Prinzhofer A, Deville E. Hydrogen emanations in intracratonic areas: new guide lines for early exploration basin screening. Geosciences 2021;11(3):145.
[27] Bultreys T, De Boever W, Cnudde V. Imaging and image-based fluid transport modeling at the pore scale in geological materials: a practical introduction to the current state-of-the-art. Earth Sci Rev 2016;155:93–128.
[28] Cnudde V, Boone MN. High-resolution X-ray computed tomography in geosciences: a review of the current technology and applications. Earth Sci Rev 2013;123:1–17.
[29] Hanna RD, Ketcham RA. X-ray computed tomography of planetary materials: a primer and review of recent studies. Chem Erde 2017;77(4):547–72.
[30] Ketcham RA, Carlson WD. Acquisition, optimization and interpretation of x-ray computed tomographic imagery: applications to the geosciences. Comput Geosci 2001;27(4):381–400.
[31] Mascini A, Boone M, Van Offenwert S, Wang S, Cnudde V, Bultreys T. Fluid invasion dynamics in porous media with complex wettability and connectivity. Geophys Res Lett 2021;48(22):e2021GL095185.
[32] Boone M, Dewanckele J, Boone M, Cnudde V, Silversmit G, Van Ranst E, Jacobs P, Vincze L, Van Hoorebeke L. Three-dimensional phase separation and identification in granite. Geosphere 2011;7(1):79–86.
[33] Laforce B, Masschaele B, Boone MN, Schaubroeck D, Dierick M, Vekemans B, Walgraeve C, Janssen C, Cnudde V, Van Hoorebeke L, Vincze L. Integrated three-dimensional Microanalysis combining X-ray microtomography and X-ray fluorescence methodologies. Anal Chem 2017;89(19):10617–24.
[34] Arif M, Mahmoud M, Zhang Y, Iglauer S. X-ray tomography imaging of shale microstructures: a review in the context of multiscale correlative imaging. Int J Coal Geol 2021;233(November 2020):103641.
[35] De Boever W, Derluyn H, Van Loo D, Van Hoorebeke L, Cnudde V. Data-fusion of high resolution X-ray CT, SEM and EDS for 3D and pseudo-3D chemical and structural characterization of sandstone. Micron 2015;74:15–21.
[36] Menke HP, Bijeljic B, Blunt MJ. Dynamic reservoir-condition microtomography of reactive transport in complex carbonates: effect of initial pore structure and initial brine pH. Geochem Cosmochim Acta 2017;204:267–85.
[37] Pearce JK, Dawson GKW, Golab A, Knuefing L, Sommacal S, Rudolph V, Golding SD. A combined geochemical and MCT study on the CO2 reactivity of Surat Basin reservoir and cap-rock cores: porosity changes, mineral dissolution and fines migration. Int J Greenh Gas Control 2019;80:10–24.
[38] Saif T, Lin Q, Butcher AR, Bijeljic B, Blunt MJ. Multi-scale multi-dimensional microstructure imaging of oil shale pyrolysis using X-ray micro-tomography, automated ultra-high resolution SEM, MAPS Mineralogy and FIB-SEM. Appl Energy 2017;202:628–47.
[39] Saur H, Sénéchal P, Boiron T, Aubourg C, Derluyn H, Moonen P. First investigation of quartz and calcite shape fabrics in strained shales by means of X-ray tomography. J Struct Geol 2020;130(130):103905.
[40] Wheatland JAT, Spencer KL, Droppo IG, Carr SJ, Bushby AJ. Development of novel 2D and 3D correlative microscopy to characterise the composition and multiscale structure of suspended sediment aggregates. Continent Shelf Res 2020;200:104112.
[41] Gualda GAR, Rivers M. Quantitative 3D petrography using x-ray tomography: application to Bishop Tuff pumice clasts. J Volcanol Geoth Res 2006;154(1–2):48–62.
[42] Créon L, Levresse G, Remusat L, Bureau H, Créon L, Levresse G, Remusat L, Bureau H, New GC, Créon L, Levresse G, Remusat L, Bureau H. New method for initial composition determination of crystallized silicate melt inclusions. Chem Geol 2020;483:162–73.
[43] Warlo M, Bark G, Wanhainen C, Butcher AR, Forsberg F, Lycksam H, Kuva J. Multi-scale X-ray computed tomography analysis to aid automated mineralogy in ore geology research. Front Earth Sci 2021;9(December):1–24.
[44] Combaudon V, Sissmann O, Bernard S, Viennet JC, Megevand V, Le Guillou C, Deville E. Are the Fe-rich-clay veins in the igneous rock of the Kansas (USA) Precambrian crust of magmatic origin? Lithos 2024;474:107583.
[45] Dhaene J, Pauwels E, De Schryver T, De Muynck A, Dierick M, Van Hoorebeke L. A realistic projection simulator for laboratory based X-ray micro-CT. Nucl Instrum Methods Phys Res Sect B Beam Interact Mater Atoms 2015;342:170–8.
[46] Dragonfly. Comet Technologies Canada inc.. 2 [Computer software]. 2022. Montreal, Canada; software available at: https://www.theobjects.com/dragonfly.
[47] Sezey M, Adun P. Validation of mohr titration method to determine salt in olive and olive brine. J. Turkish Chem. Soc. Sec. A: Chemistry 2019;6(3):329–34.
[48] Hey MH. The determination of ferrous and ferric iron in rocks and minerals; and a note on sulphosalicylic acid as a reagent for Fe and Ti. Mineral Mag 1982;46(338):111–8.
[49] Whipple ER. A study of Wilson's determination of ferrous iron in silicates. Chem Geol 1974;14(3):223–38.
[50] Yokoyama T, Nakamura E. Precise determination of ferrous iron in silicate rocks. Geochem Cosmochim Acta 2002;66(6):1085–93.
[51] Lévy D, Boka-Mene M, Meshi A, Fejza I, Guermont T, Hauville B, Pelissier N. Looking for natural hydrogen in Albania and Kosova. Front Earth Sci 2023;11:1167634.
[52] Abrajano TA, Sturchio NC, Bohlke JK, Lyon GL, Poreda RJ, Stevens CM. Methane-hydrogen gas seeps, Zambales Ophiolite, Philippines: deep or shallow origin? Chem Geol 1988;71(1–3):211–22.
[53] Arai S, Kadoshima K, Morishita T, Arai S, Kadoshima K, Morishita T. Widespread arc-related melting in the mantle section of the northern Oman ophiolite as inferred from detrital chromian spinels. J Geol Soc 2006;163(5):869–79.
[54] Boreham CJ, Edwards DS, Czado K, Rollet N, Wang L, van der Wielen S, Champion D, Blewett R, Feitz A, Henson PA. Hydrogen in Australian natural gas: occurrences, sources and resources. The APPEA J. 2021;61(1):163–91.
[55] Deville E, Prinzhofer A. The origin of N2-H2-CH4-rich natural gas seepages in ophiolitic context: a major and noble gases study of fluid seepages in New Caledonia. Chem Geol 2016;440:139–47.

[56] Donzé FV, Truche L, Namin PS, Lefeuvre N, Bazarkina EF. Migration of natural hydrogen from deep-seated sources in the São Francisco basin, Brazil. Geosciences 2020;10(9):346.
[57] Donzé FV, Tsopela A, Guglielmi Y, Henry P, Gout C. Fluid migration in faulted shale rocks: channeling below active faulting threshold. Euro. J. Environ. Civil Eng. 2020;27(8):2587–601.
[58] Ellison ET, Templeton AS, Zeigler SD, Mayhew LE, Kelemen PB, Matter JM. Low-temperature hydrogen formation during aqueous alteration of serpentinized peridotite in the samail ophiolite. J Geophys Res Solid Earth 2021;126(6): e2021JB021981.
[59] Etiope G, Samardžić N, Grassa F, Hrvatović H, Miošić N, Skopljak F. Methane and hydrogen in hyperalkaline groundwaters of the serpentinized Dinaride ophiolite belt, Bosnia and Herzegovina. Appl Geochem 2017;84:286–96.
[60] Frery E, Langhi L, Maison M, Moretti I. Natural hydrogen seeps identified in the north perth basin, western Australia. Int J Hydrogen Energy 2021;46(61): 31158–73.
[61] Hosgörmez H. Origin of the natural gas seep of Çirali (Chimera), Turkey: site of the first Olympic fire. J Asian Earth Sci 2007;30(1).
[62] Hosgormez H, Etiope G, Yalçin MN. New evidence for a mixed inorganic and organic origin of the Olympic Chimaera fire (Turkey): a large onshore seepage of abiogenic gas. Geofluids 2008;8(4):263–73.
[63] Krumrei TV, Pernicka E, Kaliwoda M, Markl G. Volatiles in a peralkaline system: abiogenic hydrocarbons and F-Cl-Br systematics in the naujaite of the Ilímaussaq intrusion, South Greenland. Lithos 2007;95(3–4).
[64] Larin N, Zgonnik V, Rodina S, Deville E, Prinzhofer A, Larin VN. Natural molecular hydrogen seepage associated with surficial, rounded depressions on the European craton in Russia. Nat Resour Res 2015;24(3):369–83.
[65] Lollar BS, Tullis CO, Lacrampe-couloume G, Ballentine C. The contribution of the Precambrian continental lithosphere to global H2 production. Nature 2014;516 (7531):379–82.
[66] Malvoisin B, Brantut N, Kaczmarek MA. Control of serpentinisation rate by reaction-induced cracking. Earth Planet Sci Lett 2017;476:143–52.
[67] Maravelis AG, Koukounya A, Tserolas P, Pasadakis N, Zelilidis A. Geochemistry of upper miocene-lower pliocene source rocks in the hellenic fold and thrust belt, zakynthos island, ionian sea, western Greece. Mar Petrol Geol 2015;66:217–30.
[68] Marks MAW, Markl G. A global review on agpaitic rocks. Earth Sci Rev 2017;173: 229–58.
[69] Milesi V, Prinzhofer A, Guyot F, Benedetti M, Rodrigues R. Contribution of siderite-water interaction for the unconventional generation of hydrocarbon gases in the Solimões basin, north-west Brazil. Mar Petrol Geol 2016:71.
[70] Moretti I, Geymond U, Pasquet G, Aimar L, Rabaute A. Natural hydrogen emanations in Namibia: field acquisition and vegetation indexes from multispectral satellite image analysis. Int J Hydrogen Energy 2022;47(84):35588–607.
[71] Moretti I, Prinzhofer A, Françolin J, Pacheco C, Rosanne M, Rupin F, Mertens J. Long-term monitoring of natural hydrogen superficial emissions in a brazilian cratonic environment. Sporadic large pulses versus daily periodic emissions. Int J Hydrogen Energy 2021;46(5):3615–28.
[72] Myagkiy A, Moretti I, Brunet F. Space and time distribution of subsurface H2concentration in so-called “fairy circles”: insight from a conceptual 2-D transport model. BSGF - Earth Sci. Bull. 2020;191(13):13.
[73] Neal C, Stanger G. Hydrogen generation from mantle source rocks in Oman. Earth Planet Sci Lett 1983;66:315–20.
[74] Nivin VA. Occurrence forms, composition, distribution, origin and potential hazard of natural hydrogen–hydrocarbon gases in ore deposits of the Khibiny and Lovozero massifs: a review. Minerals 2019;9(9):535.
[75] Potter J, Salvi S, Longstaffe FJ. Abiogenic hydrocarbon isotopic signatures in granitic rocks: identifying pathways of formation. Lithos 2013:182–3.
[76] Prinzhofer A, Tahara Cissé CS, Diallo AB. Discovery of a large accumulation of natural hydrogen in Bourakebougou (Mali). Int J Hydrogen Energy 2018;43(42): 19315–26.
[77] Salvi S, Williams-Jones AE. Reduced orthomagmatic C-O-H-N-NaCl fluids in the Strange Lake rare-metal granitic complex, Quebec/Labrador, Canada. Euro. J. Mineral., Euro. J. Mineral. 1992;4(5):1155–74.
[78] Salvi S, Williams-Jones AE. Alteration, HFSE mineralisation and hydrocarbon formation in peralkaline igneous systems: insights from the Strange Lake Pluton, Canada. Lithos 2006;91(1–4):19–34.
[79] Sano Y, Urabe A, Wakita H, Wushiki H. Origin of hydrogen-nitrogen gas seeps, Oman. Appl Geochem 1993;8(1):1–8.
[80] Ulrich M, Picard C, Guillot S, Chauvel C, Cluzel D, Meffre S. Multiple melting stages and refertilization as indicators for ridge to subduction formation: the New Caledonia ophiolite. Lithos 2010;115(1–4).
[81] Vitale Brovarone A, Martinez I, Elmaleh A, Compagnoni R, Chaduteau C, Ferraris C, Esteve I. Massive production of abiotic methane during subduction evidenced in metamorphosed ophicarbonates from the Italian Alps. Nat Commun 2017;8:1–13.
[82] Klein F, Grozeva NG, Seewald JS, McCollom TM, Humphris SE, Moskowitz B, Berquó TS, Kahl WA. Fluids in the Crust. Experimental constraints on fluid-rock reactions during incipient serpentinization of harzburgite. Am Mineral 2015;100 (4):991–1002.
[83] McCollom TM, Klein F, Moskowitz B, Solheid P. Experimental serpentinization of iron-rich olivine (hortonolite): implications for hydrogen generation and secondary mineralization on Mars and icy moons. Geochem Cosmochim Acta 2022;335: 98–110.
[84] McCollom TM, Klein F, Ramba M. Hydrogen generation from serpentinization of iron-rich olivine on Mars, icy moons, and other planetary bodies. Icarus 2022;372: 114754.
[85] Arrouvel C, Prinzhofer A. Genesis of natural hydrogen: new insights from thermodynamic simulations. Int J Hydrogen Energy 2021;46(36):18780–94.
[86] Milesi V, Prinzhofer A, Guyot F, Brunet F, Richard L, Dairou J, Benedetti AM, Millán I, Breitenach S, Meckler N, Ziegler M, Bernasconi SM. Unconventional generation of hydrocarbons in petroleum basin: the role of siderite/water interface A new calibration of the carbonate clumped isotope thermometer based on synthetic calcites. Mineral Mag 2013;77:1661–817.
[87] Milesi V, Guyot F, Brunet F, Richard L, Recham N, Benedetti M, Dairou J, Prinzhofer A. Formation of CO2, H2 and condensed carbon from siderite dissolution in the 200-300°C range and at 50MPa. Geochem Cosmochim Acta 2015;154:201–11.
[88] Bernard C, Estrade G, Salvi S, Béziat D, Smith M. Alkali pyroxenes and amphiboles: a window on rare earth elements and other high field strength elements behavior through the magmatic-hydrothermal transition of peralkaline granitic systems. Contrib Mineral Petrol 2020;175(9):1–27. 175.
[89] Bird S. Niches of the pre-photosynthetic biosphere and geologic preservation of Earth’s earliest ecology. Geobiology 2007;5(2):101–17.
[90] Murray J, Clément A, Fritz B, Schmittbuhl J, Bordmann V, Fleury JM. Abiotic hydrogen generation from biotite-rich granite: a case study of the Soultz-sous-Forêts geothermal site, France. Appl Geochem 2020;119:104631.
[91] Geymond U, Briolet T, Combaudon V, Sissmann O, Martinez I, Duttine M, Moretti I. Reassessing the role of magnetite during natural hydrogen generation. Front Earth Sci 2023;11(April):1–11.
[92] Kibleur P, Blykers B, Boone MN, Van Hoorebeke L, Van Acker J, Van den Bulcke J. Detecting thin adhesive coatings in wood fiber materials with laboratory-based dual-energy computed tomography (DECT). Sci Rep 2022;12(1):1–9.
[93] Moonen P, Dhaene J, Van den Bulcke J, Boone MN, Van Hoorebeke L. Calibration-free retrieval of density information from computed tomography data. Precis Eng 2022;76:377–84.
[94] Johnson TRC, Krauß B, Sedlmair M, Grasruck M, Bruder H, Morhard D, Fink C, Weckbach S, Lenhard M, Schmidt B, Flohr T, Reiser MF, Becker CR. Material differentiation by dual energy CT: initial experience. Eur Radiol 2007;17:1510–7.
[95] Tsuchiyama A, Nakano T, Uesugi K, Uesugi M, Takeuchi A, Suzuki Y, Noguchi R, Matsumoto T, Matsuno J, Nagano T, Imai Y, Nakamura T, Ogami T, Noguchi T, Abe M, Yada T, Fujimura A. Analytical dual-energy microtomography: a new method for obtaining three-dimensional mineral phase images and its application to Hayabusa samples. Geochem Cosmochim Acta 2013;116:5–16.
[96] Godinho JRA, Westaway-Heaven G, Boone MA, Renno AD. Spectral tomography for 3d element detection and mineral analysis. Minerals 2021;11(6):598.
[97] Sittner J, Godinho JRA, Renno AD, Cnudde V, Boone M, De Schryver T, Van Loo D, Merkulova M, Roine A, Liipo J. Spectral X-ray computed micro tomography: 3-dimensional chemical imaging. X Ray Spectrom 2021;50(2):92–105.